Nanoscale

PAPER

View Article Online
View Journal | View Issue

Cite this: *Nanoscale*, 2014, 6, 11431

Cluster-size dependent internal dynamics and magnetic anisotropy of Ho ions in $HoM_2N@C_{80}$ and $Ho_2MN@C_{80}$ families (M = Sc, Lu, Y)†

Y. Zhang,[a] D. Krylov,[a] S. Schiemenz,[a] M. Rosenkranz,[a] R. Westerström,[bc] J. Dreiser,[cd] T. Greber,[b] B. Büchner[a] and A. A. Popov*[a]

Received 27th May 2014
Accepted 25th July 2014

DOI: 10.1039/c4nr02864c

www.rsc.org/nanoscale

The paramagnetic NMR study of $HoM_2N@C_{80}$-I_h and $Ho_2MN@C_{80}$-I_h nitride cluster fullerenes (M = Sc, Lu, Y) reveals strong dependence of Ho-induced paramagnetic shifts (δ^{para}) in ^{13}C NMR spectra on the size of the diamagnetic metal in the cluster. In particular, the δ^{para} value in $HoY_2N@C_{80}$ is almost doubled in comparison to that in $HoSc_2N@C_{80}$. X-ray magnetic circular dichroism studies show that all Ho–nitride cluster fullerenes have the same magnetic ground state of Ho^{3+}. Point-charge ligand-field splitting calculations show that the increase of the M^{3+} radius in going from Sc to Y results in a considerable increase of the energy splitting between different J_z states. This leads to a 19% higher magnetic anisotropy of Ho^{3+} in $HoY_2N@C_{80}$ than in $HoSc_2N@C_{80}$ at 300 K. Variations of the molecular geometry and cluster dynamics with the size of the cluster are found to have even greater influence on δ^{para} values. This work shows that the magnetic properties of the species confined inside the fullerene cages can be tuned using the geometrical factors such as the cluster and the cage size.

Introduction

Endohedral fullerenes are versatile in terms of their ability to encapsulate different types of metal atoms and clusters as well as protect unusual endohedral species and their charge and spin states from the outer environment.[1,2] Nitride cluster fullerenes (NCFs) with the formulae $M_3N@C_{2n}$ (M = Sc, Y, lanthanides; $2n = 68$–96) are particularly attractive because of their stability, reasonable production yield and possibility to alter the composition of the internal cluster combining two or even three different metal atoms within one NCF molecule.[3–5] Endohedral fullerenes encapsulating lanthanide ions attract enhanced attention because of their distinct magnetic properties.[6–20] Recent discovery of single molecular magnetic behaviour in the $Dy_xSc_{3-x}N@C_{80}$-I_h ($x = 1$–3) series[12,19] calls for more detailed studies of NCF encapsulating lanthanide ions with large magnetic anisotropy.

In addition to its protective role, the carbon cage is also a natural limiter of the cluster size.[21] Therefore, encapsulation of ions of different size within the same carbon cage alters internal geometrical parameters of the cluster such as metal–nitrogen distances.[22–25] In due turn, geometrical changes can be used to tune the physicochemical properties of encapsulated ions. For instance, confinement of the CeM_2N and Ce_2MN clusters (M = Sc, Y, Lu) within the fullerene cages of different size was used to vary the redox properties of the Ce(IV)/Ce(III) redox couple in Ce-based NCFs.[24,26] From the point of view of the lanthanide-based magnetism, a variation of geometrical parameters of the nitride cluster is expected to vary the ligand field and the magnetic exchange coupling between lanthanide ions. In this work we use this strategy to study the effect of the cluster size variation on the magnetic properties of Ho-based NCFs. The series of $HoM_2N@C_{80}$-I_h and $Ho_2MN@C_{80}$-I_h NCFs (M = Sc, Y, Lu) are synthesized with progressively increasing radii of diamagnetic metal ions (Shannon radii of Sc^{3+}, Lu^{3+}, and Y^{3+} are 0.745, 0.86, and 0.90 Å, respectively[27]). The J_z state of Ho is addressed by means of X-ray magnetic circular dichroism (XMCD) and paramagnetic ^{13}C NMR techniques. The magnetic anisotropies are rationalized with model calculations of the ligand field splitting and molecular dynamics of the endohedral cluster.

Results and discussion

Synthetic procedures

Ho/Lu and Ho/Y mixed-metal NCFs were synthesized by arc-discharge synthesis using corresponding metal oxides and guanidine thiocyanate as a source of nitrogen. After dc-arc

---

[a] *Leibniz-Institute for Solid State and Materials Research (IFW Dresden), D-01171 Dresden, Germany. E-mail: a.popov@ifw-dresden.de*
[b] *Physik-Institut, Universität Zürich, 8057 Zürich, Switzerland*
[c] *Swiss Light Source, Paul Scherrer Institut, 5232 Villigen PSI, Switzerland*
[d] *Institute of Condensed Matter Physics, Ecole Polytechnique Fédérale de Lausanne, CH-1015 Lausanne, Switzerland*

† Electronic supplementary information (ESI) available: Details of the synthesis, separation, spectroscopic characterization, and quantum chemical computations. See DOI: 10.1039/c4nr02864c

discharging, the soot was pre-extracted with acetone and further Soxhlet-extracted with CS_2. Separation of fullerene extracts was accomplished by two-step high pressure liquid chromatography. Details of synthesis and separation procedures as well as spectroscopic characterization of NCFs are described in the ESI.† Synthesis and separation of $HoSc_2N@C_{80}$-I_h and $Ho_2ScN@C_{80}$-I_h were reported by us previously.[28] Fig. 1 shows mass-spectra and schematic molecular structure of all isolated compounds. Note that complete separation of $HoLu_2N@C_{80}$-I_h from $Lu_3N@C_{80}$-I_h was not possible without significant loss of the material, and hence the sample used for NMR studies contained *ca.* 20% of $Lu_3N@C_{80}$-I_h.

NMR spectroscopic studies

A highly symmetric C_{80}-I_h cage has only two types of carbon atoms, 60 atoms on pentagon–hexagon–hexagon junctions (PHHJs) and 20 atoms on triple hexagon junctions (THJs). Although the symmetry of the M_3N cluster is much lower than that of the carbon cage, at room temperature the cluster in $M_3N@C_{80}$-I_h rotates rapidly on the NMR time scale, and carbon NMR signals are averaged.[29,30] Accordingly, ^{13}C NMR spectra of diamagnetic $M_3N@C_{80}$-I_h NCFs exhibit two sharp lines at 144 and 137–138 ppm in a 3 : 1 ratio, respectively. Variations of these chemical shifts for different cluster compositions within the set of diamagnetic metal ions (Sc, Y, Lu) do not exceed 1 ppm.[31]

Fig. 2 shows 125 MHz ^{13}C NMR spectra of the $HoM_2N@C_{80}$ and $Ho_2MN@C_{80}$ series measured at room temperature in CS_2 solution (the samples were thermostatted and the temperature variation during the measurements was in the range of 300 ± 0.1 K). Diamagnetic $Lu_3N@C_{80}$-I_h present in the $HoLu_2M@C_{80}$-I_h sample exhibits two sharp ^{13}C signals at 144.3 and 137.6 ppm (Fig. 2a), as expected for diamagnetic $M_3N@C_{80}$-I_h NCFs. Replacement of one diamagnetic metal atom in $M_3N@C_{80}$-I_h with Ho dramatically changes ^{13}C NMR spectra. First, the relaxation time becomes very short and the spectral lines are substantially broadened (from less than 0.2 ppm to *ca.* 5 ppm). This broadening results in a decrease of the signal-to-noise ratio and requires a much longer acquisition time. After 10 days of acquisition, only higher intensity PHHJ signals can be identified unambiguously, whereas positions of THJ signals are not so well defined because of lower intensity and poor signal to noise ratio. Second, the presence of paramagnetic Ho^{3+} ions shifts ^{13}C peaks of $HoM_2N@C_{80}$-I_h to a higher field in comparison to signals of diamagnetic $M_3N@C_{80}$-I_h NCFs. PHHJ signals are found at 119 ppm (M = Sc), 107 ppm (M = Lu), and 101 ppm (M = Y), whereas tentative positions of THJ signals are determined to be 74 ppm (Sc), 66 ppm (Lu), and 76 ppm (Y). We define the Ho-induced paramagnetic shift, δ^{para}, as $\delta^{exp} - \delta^{dia}$, where δ^{exp} is the measured value and δ^{dia} is the chemical shift in analogous diamagnetic NCFs. Surprisingly, δ^{para} depends strongly on the second metal. For PHHJ signals, the shift increases systematically with the size of the M^{3+} ion (Shannon radii of Sc^{3+}, Lu^{3+}, and Y^{3+} are 0.745, 0.86, and 0.90 Å, respectively[27]). The difference of the PHHJ peak positions between $HoSc_2N@C_{80}$ and $HoY_2N@C_{80}$, 18 ppm, is almost as large as the 25 ppm difference between PHHJ signals of $HoSc_2N@C_{80}$ and diamagnetic $LuSc_2N@C_{80}$.

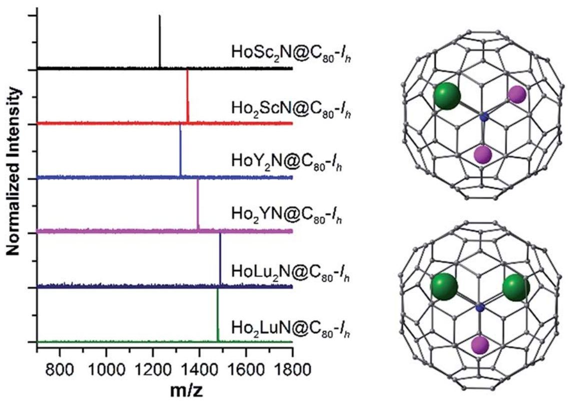

Fig. 1 Laser desorption ionization mass-spectra of $HoM_2N@C_{80}$-I_h and $Ho_2MN@C_{80}$-I_h NCFs (M = Sc, Y, Lu) and schematic description of their molecular structures (Ho is green and diamagnetic metals are magenta).

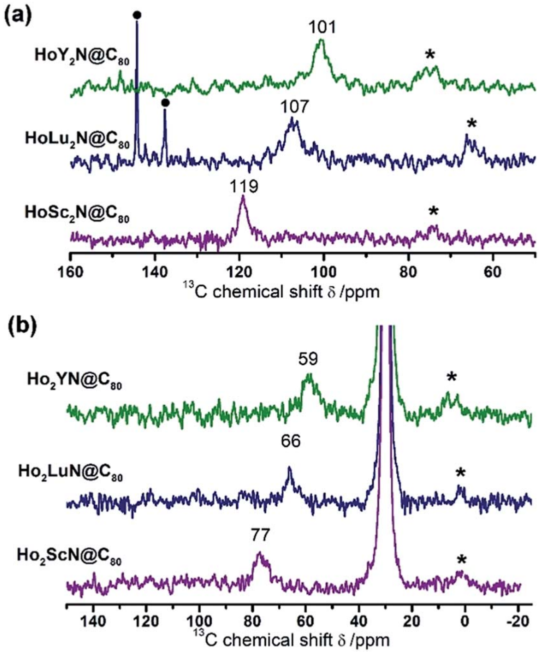

Fig. 2 ^{13}C NMR spectra of $HoM_2N@C_{80}$-I_h and $Ho_2MN@C_{80}$-I_h NCFs (M = Sc, Y, Lu) measured in CS_2 solution. PHHJ signals are marked with their chemical shifts, prospective THJ signals are marked with asterisks, and signals of $Lu_3N@C_{80}$ present in the $HoLu_2N@C_{80}$ sample are marked with dots. A strong signal near 30 ppm in (b) is due to the deuterated acetone.

When the second Ho ion is introduced into the nitride cluster, paramagnetic shifts are further increased. In comparison to $Lu_2ScN@C_{80}$,[31] the PHHJ signal of $Ho_2ScN@C_{80}$ is shifted to a higher field ($\delta^{para} = -67$ ppm), and even larger shifts are observed for $Ho_2LuN@C_{80}$ ($\delta^{para} = -78$ ppm) and $Ho_2YN@C_{80}$ ($\delta^{para} = -85$ ppm). THJ signals are also found at a higher field with tentative peak positions of 2 ppm for $Ho_2ScN@C_{80}$, 2 ppm for $Ho_2LuN@C_{80}$, and 5 ppm for $Ho_2YN@C_{80}$.

Although large Ho-induced paramagnetic shifts are anticipated, the fact that they are strongly dependent on the size of the diamagnetic metal in the cluster is rather surprising and requires deeper analysis. In solution, a paramagnetic shift has two major contributions caused by contact (Fermi) interactions and dipolar interactions.[32] The contact shift (δ^{con}) results from the interaction between the nuclear spin and electron spin density located at the atom of interest (*i.e.* carbon). In other words, this term appears when the spin density is "leaked" from the paramagnetic center to other atoms in the molecule. The dipolar shift (also termed as pseudocontact, δ^{pc}) is caused by the through-space interactions of magnetic dipoles. For a molecule in solution, the dipolar term should vanish unless the paramagnetic center has magnetic anisotropy. According to Bleaney theory,[33,34] contact and pseudocontact terms can be distinguished by their temperature dependence: δ^{con} has T^{-1} dependence whereas the main temperature dependent term in δ^{pc} scales as T^{-2} (note that some deviations from the T^{-2} dependence were also reported[35–38] and are attributed to a main drawback of Bleaney's theory, an assumption of the ligand field splitting being smaller than k_BT).

Unfortunately, variable temperature ^{13}C NMR studies of Ho–NCFs are too demanding at this moment. Besides Ho–NCFs, paramagnetic shifts in the ^{13}C NMR spectra of nitride cluster fullerenes were reported for a series of $CeM_2N@C_{80}$-I_h compounds (M = Sc, Y, Lu).[24,39] Paramagnetic shifts of $CeM_2N@C_{80}$-I_h are much smaller (2–3 ppm) which is not surprising taking into account much smaller magnetic moment of Ce^{3+} ($4f^1$, $J = 5/2$) in comparison to Ho^{3+} ($4f^{10}$, $J = 8$). More importantly, ^{13}C NMR signals of $CeM_2N@C_{80}$-I_h are much narrower, and their temperature dependence could be studied more straightforwardly. The pseudocontact shift in $CeM_2N@C_{80}$-I_h[24,39,40] and other Ce-EMFs[41–43] was found to be dominant, which agrees well with the "buried" nature of unpaired 4f electrons in lanthanide ions. Besides, analysis of the temperature dependence of the ^{45}Sc NMR signal of $HoSc_2N@C_{80}$-I_h reported previously[28] also proved that the paramagnetic shift is largely due to dipolar interactions of the 4f electrons with the electrons in the carbon cage. Based on these data, in this work we focus only on the pseudocontact term.

The pseudocontact shift for a given carbon atom in $HoM_2N@C_{80}$ can be computed as.

$$\delta^{\text{pc}} = \frac{(3\cos^2\theta - 1)}{12\pi R^2}(\chi_{\parallel} - \chi_{\perp}) \qquad (1)$$

where R is the distance between carbon and Ho atoms, θ is the angle between the Ho–C vector and the quantization axis z (taken along the Ho–N vector, see below), whereas $\chi_{\parallel}$ and $\chi_{\perp}$ are parallel and perpendicular components of the magnetic susceptibility tensor of Ho^{3+} ions in the $HoM_2N@C_{80}$ molecule with respect to the z axis.[32] Eqn (1) shows that the dependence of the ^{13}C paramagnetic shift on the radius of M^{3+} ions can be caused by two reasons: (i) variation of the magnetic susceptibility and (ii) geometrical factor, *i.e.* variation of the molecular geometry and hence $\cos^2\theta$ and/or R. Note that because of the cluster rotation, the measured chemical shifts are averaged over all carbon atoms and hence the geometrical factor includes not only atomic coordinates in the energy minimum, but also the influence of the cluster size on its dynamics inside the cage.

X-ray magnetic circular dichroism

To clarify whether the magnetic properties of Ho ions are not identical in different $HoM_2N@C_{80}$ and $Ho_2MN@C_{80}$ NCFs, we studied XMCD spectra at the Ho $M_{4,5}$ edges. Ho–NCF samples were drop cast onto a polycrystalline aluminum sample plate and the spectra were recorded at ∼4 K and a magnetic field of ±6.5 T (magnetization of the samples at room temperature was too small for reliable measurements). Fig. 3a shows typical X-ray absorption spectra (XAS) recorded with right and left circularly polarized light as well as total XAS ($I^+ + I^-$) and XMCD ($I^+ - I^-$). XMCD spectra of all 6 Ho–NCFs (Fig. 3b) are virtually identical. The expectation values of spin and angular momenta $\langle S_z \rangle$ and $\langle L_z \rangle$ (Table 1) computed using sum rules[12,44,45] are also rather close within their uncertainty ranges. These results show that the single ion J_z ground state of Ho^{3+} in all studied NCFs is the same. $\langle J_z \rangle$ values estimated as the sum of $\langle S_z \rangle$ and $\langle L_z \rangle$ are close to 4, which is expected for a rotationally averaged ground state with $m_J = \pm 8$. These data are in line with the recent SQUID study of $HoSc_2N@C_{80}$ which proved that the ground magnetic state of Ho^{3+} in this metallofullerene is $|m_J| = 8$.[46]

Ligand-field splitting in $HoM_2N@C_{80}$

The ligand field lifts the degeneracy of the Ho $4f^{10}$ state into different J_z levels. In contrast to low-temperature XMCD data, NMR measurements are performed at room temperature, where the influence of excited states becomes prominent. This requires the analysis of the ligand-field (LF) splitting. Here we will consider $HoSc_2N@C_{80}$ and $HoY_2N@C_{80}$ molecules as having the smallest and largest diamagnetic metal ions. The increase of the M^{3+} radius in the $HoM_2N@C_{80}$ cluster increases the M–N bond length and in turn shortens the Ho–N distance. At the B3LYP level with 4f-in-core potential in the Firefly code,[47] the Ho–N bond length drops from 2.163 Å in $HoSc_2N@C_{80}$ to 2.067 Å in $HoY_2N@C_{80}$. It is reasonable to consider that the

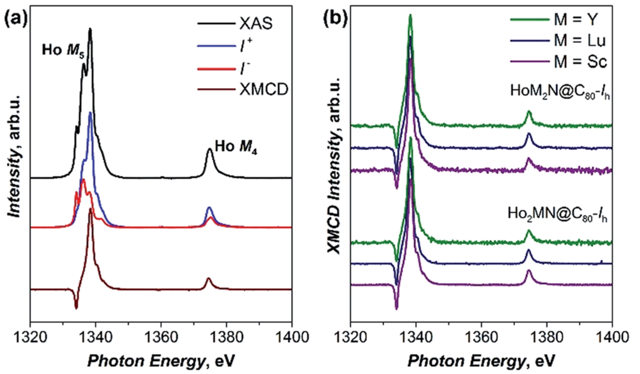

Fig. 3 (a) X-ray absorption spectra of $Ho_2ScN@C_{80}$-I_h at the $M_{4,5}$ edge (3d → 4f excitations) recorded with right and left circular polarized light (I^+ and I^-) as well as total XAS ($I^+ + I^-$) and XMCD ($I^+ - I^-$); (b) normalized XMCD spectra of $HoM_2N@C_{80}$-I_h and $Ho_2MN@C_{80}$-I_h NCFs.

Table 1 Ho spin and orbital angular momenta of Ho–NCFs obtained from XMCD spectra using sum rules[a]

	$HoM_2N@C_{80}$		$Ho_2MN@C_{80}$	
M	$\langle S_z \rangle$	$\langle L_z \rangle$	$\langle S_z \rangle$	$\langle L_z \rangle$
Sc	1.22 ± 0.20	2.71 ± 0.22	1.13 ± 0.02	2.54 ± 0.01
Lu	1.32 ± 0.11	2.80 ± 0.24	1.26 ± 0.05	2.76 ± 0.12
Y	1.25 ± 0.12	2.75 ± 0.29	1.23 ± 0.11	2.62 ± 0.22

[a] Expectation value of the Ho dipole operator $\langle T_z \rangle$ was evaluated according to eqn (8) in ref. 45.

highly charged nitrogen ion makes the main contribution to the ligand-field and hence the variation of the Ho–N distance must affect the splitting of the J_z levels of the Ho^{3+} ion.

To estimate the LF splitting of the $^5I_8$ manifold of Ho^{3+} ($4f^{10}$) we used a point-charge code *so1ion (Cfield)* implemented in the McPhase[48] program. Atomic charges were computed by integration of the total density in the framework of Bader's QTAIM method.[49] In view of the similarity of ionic radii of Y and Ho, $YSc_2N@C_{80}$ was used in these calculations as a model for $HoSc_2N@C_{80}$ and $DySc_2N@C_{80}$, whereas $Y_3N@C_{80}$ was used as a model for $HoY_2N@C_{80}$ (ionic radii of Y^{3+} and Ho^{3+} are almost identical). The structures were optimized at the PBE level for consistency with molecular dynamics simulations discussed below. Detailed analysis of the chemical bonding in endohedral metallofullerenes using the QTIAM approach was reported by us previously,[50] and in this manuscript we focus only on the atomic charges.

To verify the model, we first computed the ligand field splitting in isostructural $DySc_2N@C_{80}$-I_h and compared to the results of recently published *ab initio* CASSCF calculations.[51] These computations showed that QTAIM charges are too large, but can reproduce *ab initio* LF splitting fairy well when scaled by a factor of 0.755 (see Table 2). The same scaled charges were then used to calculate LF splitting in $HoSc_2N@C_{80}$. The values listed in Table 2 and depicted in Fig. 4 show that the overall LF splitting in $HoSc_2N@C_{80}$ is rather large and exceeds 500 cm^{-1}. In agreement with XMCD and SQUID measurements, the ground magnetic state is $|m_J| = 8$. The energy then increases systematically with the decrease of $|m_J|$ values. Ho^{3+} is not a Kramers ion and hence the degeneracy of $\pm m_J$ states is not enforced. However, our calculations show that the degeneracy holds within 1 cm^{-1} for $|m_J|$ values ranging from 8 to 3, and considerable splitting is found only for $|m_J| = 2$ (7 cm^{-1}) and $|m_J| = 1$ (23 cm^{-1}). Note that the ligand field breaks the spherical symmetry of the potential in which the 4f electrons move. Thus the m_J states are mixed, especially for small $|m_J|$ values, showing that in principle m_J is not a "good" quantum number anymore. The $|m_J|$ assignment is done according to the dominant components in the corresponding state that is linear combinations of all m_J states.

Table 2 LF splitting in $DySc_2N@C_{80}$, $HoSc_2N@C_{80}$ and $HoY_2N@C_{80}$[a]

	$DySc_2N@C_{80}$		$HoSc_2N@C_{80}$[d]		$HoY_2N@C_{80}$[e]	
±*m* Ho (Dy)	CAS-SCF[b]	PC[c]	All	N′	All	N′
8 (7.5)	0	0	0	0	0	0
7 (6.5)	372	387	186	176	232	221
6 (5.5)	729	708	299	289	368	358
5 (4.5)	1009	958	375	370	458	453
4 (3.5)	1180	1139	434	433	527	527
3 (2.5)	1268	1259	482	483	583	587
2 (1.5)	1338	1329	515/522	522	624/632	634
1 (0.5)	1401	1401	536/559	546	650/677	664
0			561	555	678	675

[a] All values in cm^{-1}. [b] CASSCF values are from ref. 51. [c] PC means the point charge model with QTAIM charges scaled by 0.755. [d] "All" means point-charge calculations for the whole molecule, N′ denotes point-charge calculations for the Ho–N fragment with the QTAIM charge of nitrogen scaled by 0.755 × 0.802. [e] The same as "All" means point-charge calculations for the whole molecule, N′ denotes point-charge calculations for the Ho–N fragment with the QTAIM charge of nitrogen but the nitrogen charge is scaled by 0.755 × 0.816.

Point-charge computations are very convenient for the analysis of the role of different intramolecular interactions in the total LF splitting since "unwanted" contributions can be turned off. As anticipated, the nitrogen ion has the greatest influence on the LF. However, LF splitting computed for the Ho–N fragment overestimates the total splitting by *ca.* 20% (note that the Ho–N system is uniaxial and the $\pm m_J$ degeneracy is rigorous). The next largest contribution is that from Sc ions. LF splitting for the $HoSc_2N$ cluster is *ca.* 10% smaller than for the whole $HoSc_2N@C_{80}$ molecule, but the overall splitting pattern (multiplet) is already very similar to the multiplet

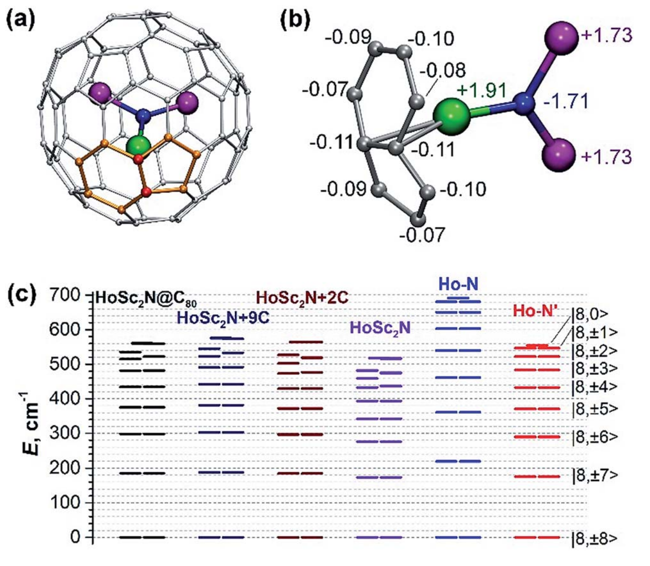

Fig. 4 (a) DFT optimized molecular structure of $HoSc_2N@C_{80}$ (N is blue, Sc is magenta, Ho is green, carbon atoms are grey except for 2 nearest atoms shown as red spheres and 9 nearest atoms highlighted in orange); (b) a fragment of the molecule with QTAIM atomic charges; (c) LF splitting computed for $HoSc_2N@C_{80}$ taking into account different intramolecular interactions: the whole molecule, $HoSc_2N$ cluster with nearest 9 and 2 carbon atoms, only $HoSc_2N$ cluster, and only Ho–N fragment (computed levels with additionally scaled charge of nitrogen are denoted as Ho–N′). |*J*, ±*m* > states in the Ho–N′ system are indicated in the rightmost column.

computed for the whole molecule. Importantly, lifting of the $\pm m_J$ degeneracy in $HoSc_2N@C_{80}$ is fairly well reproduced in $HoSc_2N$, and further inclusion of the cage carbon atoms only stretches the energy range without changing the pattern. When only two carbon atoms nearest to Ho are taken into account (they also have the largest negative QTAIM charges, Fig. 4b), the splitting energies are very close to the whole $HoSc_2N@C_{80}$ system. This is in part due to a fortuitous cancellation of contributions of different atoms since computations with 9 nearest carbon atoms give slightly larger (*ca.* 2%) splitting than for the whole system. Anyway, it can be seen that the cage carbon atoms only slightly influence the LF, whereas the main terms are caused by the nitrogen and the scandium ions. This is not surprising taking into account how small atomic charges of carbons are when compared to those of N and Sc (see Fig. 4b).

LF calculations for $HoY_2N@C_{80}$ based on the $Y_3N@C_{80}$ molecular geometry and QTAIM charges yield significantly higher splitting than in $HoSc_2N@C_{80}$ (see Fig. 5a and Table 1). For instance, in $HoY_2N@C_{80}$ the first excited state with $|m_J| = 7$ is at 232 cm^{-1}, which is 46 cm^{-1} higher than the energy of the first excited state in $HoSc_2N@C_{80}$ (186 cm^{-1}). Aside from the increased energy scale, the LF splitting pattern in $HoY_2N@C_{80}$ is similar to that in $HoSc_2N@C_{80}$. The LF splitting of $HoY_2N@C_{80}$ and $HoSc_2N@C_{80}$ scales with a factor of 1.205 (Fig. 5b). If this increase of the LF splitting is solely attributed to the shorter Ho–N distance (2.063 Å *versus* 2.160 Å), this implies that the ligand field splitting scales with the Ho–N distance R as R^{-4}. However, this empirical relationship has to be used with care, since the nominal atomic charge of the nitrogen also depends on R (−1.77 in $Y_3N@C_{80}$ *versus* −1.71 in $YSc_2N@C_{80}$). Furthermore, the atomic charges of Y in $Y_3N@C_{80}$ (+1.88) are also higher than the charges of Sc in $YSc_2N@C_{80}$ (+1.73).

Point-charge computations prove that nitrogen has the largest contribution of the ligand field in $HoM_2N@C_{80}$ molecules and show that $HoY_2N@C_{80}$ has higher LF splitting than $HoSc_2N@C_{80}$ mainly because of the shorter Ho–N distance. The ground state, a doublet with $m_J = \pm 8$, is the same for both molecules, which agrees well with low temperature XMCD measurements. The magnitude of the LF splitting (*ca.* 190–230 cm^{-1} for the first excited state) indicates that considerable differences in magnetic properties of $HoSc_2N@C_{80}$ and $HoY_2N@C_{80}$ can be expected at relatively high temperature, when excited states have considerable populations. This is reflected in room temperature ^{13}C NMR spectra. Computations of the magnetic susceptibility tensor using the Van Vleck formulae show that the $\Delta\chi$ value ($\Delta\chi = \chi_{\parallel} - \chi_{\perp}$) for $HoY_2N@C_{80}$ is 19% higher than that in $HoSc_2N@C_{80}$ at 300 K. This considerable difference is in line with the LF splitting (see above), but it cannot fully account for the 70% difference in paramagnetic shifts. Therefore, the structural factor has even greater impact on the paramagnetic shifts and will be analyzed below.

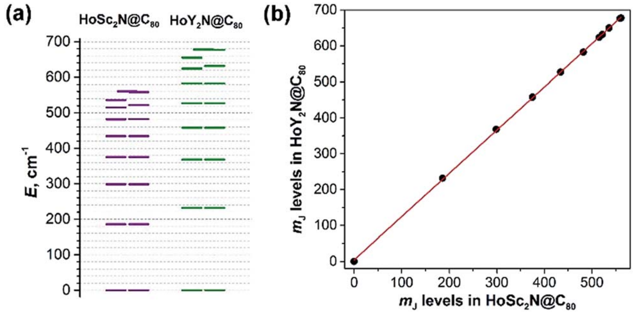

Fig. 5 (a) LF splitting computed for $HoSc_2N@C_{80}$ and $HoY_2N@C_{80}$; (b) correlation between m_J energy levels in $HoSc_2N@C_{80}$ and $HoY_2N@C_{80}$. The slope of the fitting line in (b) is 1.205.

Static computations of paramagnetic shifts

Using the anisotropy of magnetic susceptibility at 300 K and DFT-optimized coordinates, δ^{pc} values can be computed using eqn (1). The values for individual carbon atoms are huge (up to several thousands of ppm for the carbon atom close to Ho), but averaging over the whole carbon cage gives the values of −25 and −19 ppm for PHHJ and THJ carbons in $HoSc_2N@C_{80}$ and −53 (PHHJ) and −7 ppm (THJ) in $HoY_2N@C_{80}$ (Table 3). Computed values for PHHJ carbons are in good agreement with experimental values (−27 ppm in $HoSc_2N@C_{80}$ and −43 ppm in $HoY_2N@C_{80}$). Thus, the large difference in Ho-induced paramagnetic chemical shift in $HoM_2N@C_{80}$-I_h molecules should be ascribed to subtle variations of the Y-cage coordination (see also ref. 31).

The pseudocontact paramagnetic shift computed for Sc atoms in $HoSc_2N@C_{80}$ is 971 ppm, which agrees reasonably well with the experimental $\Delta\delta^{para}$ shift of 800 ppm in ^{45}Sc NMR spectra.[28] Furthermore, variable-temperature ^{45}Sc NMR measurements of $HoSc_2N@C_{80}$-I_h revealed strong temperature dependence of the signal, whose position gradually shifted from 1178 ppm at 268 K to 956 ppm at 308 K.[28] Computations of $\Delta\chi$ values at 268 and 308 K and an assumption of the weak temperature variation of the geometry-related term in eqn (1) predict that the ^{45}Sc paramagnetic shift should decrease by 285 ppm (compared to the experimentally measured decrease of 222 ppm).

Table 3 Experimental and computed paramagnetic chemical shifts δ^{para} in $HoSc_2N@C_{80}$ and $HoY_2N@C_{80}$

NCF	Nuclei	Model[a]	PHHJ	THJ
$HoSc_2N@C_{80}$	^{13}C	Exp.	−25	−70
	^{13}C	Static	−25	−19
	^{13}C	MD	−22	−24
	^{45}Sc	Exp.	800	
	^{45}Sc	Static	971	
	^{45}Sc	MD	998	
$HoY_2N@C_{80}$	^{13}C	Exp.	−43	−68
	^{13}C	Static	−53	−7
	^{13}C	MD	−46	−16

[a] $LuSc_2N@C_{80}$ and $LuY_2N@C_{80}$ from ref. 31 are used as diamagnetic references for exp. values, MD denotes the values averaged over molecular dynamics trajectories; the values for $HoY_2N@C_{80}$ are averaged over three calculations in which different Y atoms in $Y_3N@C_{80}$ were treated as Ho.

Molecular dynamics simulations

The cluster in $M_3N@C_{80}$-I_h NCFs rotates rapidly at room temperature, and hence the use of DFT-optimized coordinates for estimation of the structural factor may not be fully appropriate. Heine *et al.* showed that computations of ^{13}C shifts sampling molecular dynamic trajectory gave much better results for $Sc_3N@C_{80}$-I_h than static computations.[52] To evaluate the effect of the cluster dynamics we have performed DFT-based Born–Oppenheimer molecular dynamics (BOMD) simulations for $YSc_2N@C_{80}$ and $Y_3N@C_{80}$ molecules using the CP2K[53] code. Fig. 6 shows 50 ps trajectories of both molecules run at 300 K, and Fig. 7 shows these trajectories in polar coordinates. It can be seen that the changes of the cluster size have not a very large but distinct effect. In DFT-optimized structures Sc atoms tend to be coordinated to pentagon/hexagon edges,[31] and this tendency is clearly seen in the BOMD trajectory (Fig. 7a), where Sc positions are clustering near 5/6 edges. In the DFT-optimized $Y_3N@C_{80}$ structure Y atoms are located closer to the centers of hexagons,[31] and the positions of Y atoms in the BOMD trajectory of $Y_3N@C_{80}$ are oscillating around the centers of hexagons. The dynamic behaviour of Y in $YSc_2N@C_{80}$ is intermediate and Y positions are clustered both near the centers of hexagons and close to pentagon/hexagon edges. The Y–N bond lengths display significant variations along the trajectories (Fig. 6c and d), and the effect of dynamics on Ho^{3+} magnetic anisotropy cannot be ignored.

Point-charge calculations showed that deviation of the ligand field from the axial form is significant only for the highest energy states, which are not relevant for the room temperature measurements. For the lower states, the LF of the whole $HoM_2N@C_{80}$ molecules can be approximated by a single nitrogen atom whose atomic charge is scaled by additional factors of 0.802 (Sc) or 0.816 (Y) optimized to fit $\Delta\chi$ values computed for the whole molecules (Table 3). Employing this simplified model, the $\Delta\chi$ values were computed at 300 K at different Ho–N distances and then approximated by an analytical function (see ESI†), which then allowed estimation of $\Delta\chi$ values for all BOMD steps. Averaging ^{13}C chemical shifts for the whole trajectory yields the δ^{pc} values of −22 and −24 ppm for PHHJ and THJ carbons in $HoSc_2N@C_{80}$, respectively, which is rather close but not equal to static values (Table 3). For $HoY_2N@C_{80}$ the effect of dynamics is more enhanced: the δ^{pc} shift of PHHJ atoms is reduced to −46 ppm (static value is −53 ppm), and the THJ signal is changed to −16 ppm (from the static value of −7 ppm). For both $HoSc_2N@C_{80}$ and $HoY_2N@C_{80}$, dynamical effects are noticeable but not crucial and their use slightly improves agreement for PHHJ ^{13}C signals. Computed values for THJ carbons are still rather far from tentative experimental indications. This may be due to the non-negligible contribution of the Fermi term in paramagnetic shift.

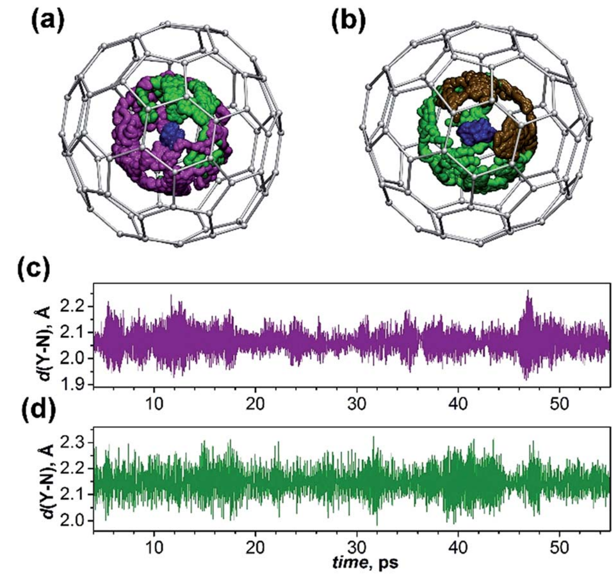

Fig. 6 (a and b) BOMD trajectories (50 ps) of $YSc_2N@C_{80}$ (a) and $Y_3N@C_{80}$ (b) computed at the PBE level at 300 K. Nitrogen is blue, Y is green, Sc is magenta. In (b) one of the Y atoms is shown in brown. Displacements of carbon atoms are not shown. (c and d) Variation of instantaneous Y–N bond lengths in $YSc_2N@C_{80}$ (c) and $Y_3N@C_{80}$ (d).

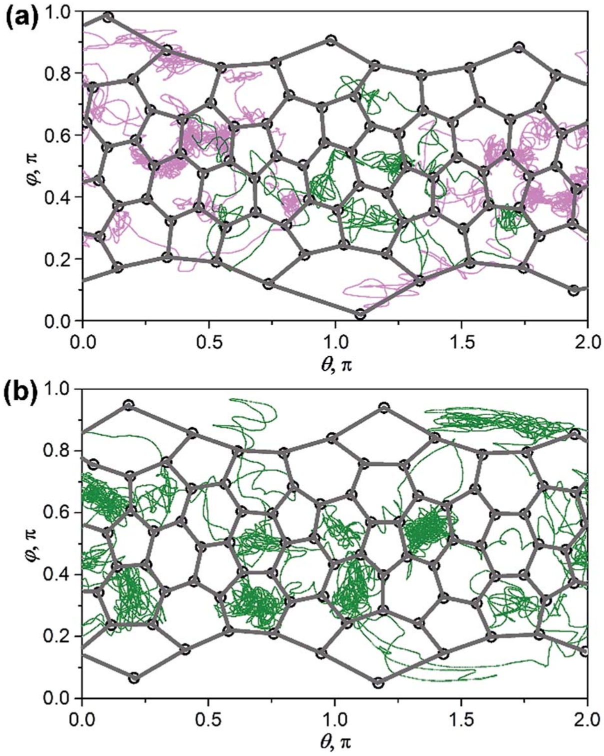

Fig. 7 BOMD trajectories of $YSc_2N@C_{80}$ (a) and $Y_3N@C_{80}$ (b) shown in polar coordinates to emphasize their rotational component. Carbon atoms are shown as black open circles connected by grey lines (C–C bonds), Y atoms are green, and Sc atoms are magenta.

Conclusions

We have shown that the variation of the cluster size in $HoM_2N@C_{80}$-I_h and $Ho_2MN@C_{80}$-I_h NCFs *via* the choice of diamagnetic metals M with different ionic radii (Sc, Lu, Y) results in considerable changes of the Ho-induced paramagnetic shift in ^{13}C NMR spectra. This unanticipated phenomenon was explained by a combination of magnetic and geometrical factors. First, shortening of the Ho–N distance results in a considerable increase of the ligand-field splitting, which yields a considerable difference in anisotropy of magnetic susceptibilities of $HoSc_2N@C_{80}$ and $HoY_2N@C_{80}$. Second, with the increase of the cluster size, the metal atoms change the way they coordinate to the cage carbon atoms. This variation is well seen in the dynamical description of the cluster motions inside the cage. Thus, using a confined state of the nitride cluster in a cage of a fixed size, we can tune the magnetic properties of encapsulated species *via* judicious choice of the cluster constituents.

Acknowledgements

This work was supported by Deutsche Forschungsgemeinschaft (projects PO 1602/1-1 to A.A.P. and DU225/31-1 within the D-A-CH program) and Swiss National Science Foundation (grant no. PZ00P2_142474). The X-ray absorption measurements were performed on the EPFL/PSI X-Treme beamline[54] at the Swiss Light Source, Paul Scherrer Institut, Villigen, Switzerland. Computational resources were provided by the Supercomputing Center of Moscow State University[55] and Center for Information Services and High Performance Computing (ZIH) in TU-Dresden.

Notes and references

1 A. A. Popov, S. Yang and L. Dunsch, *Chem. Rev.*, 2013, **113**, 5989–6113.

2 X. Lu, L. Feng, T. Akasaka and S. Nagase, *Chem. Soc. Rev.*, 2012, **41**, 7723–7760.

3 J. Zhang, S. Stevenson and H. C. Dorn, *Acc. Chem. Res.*, 2013, **46**, 1548–1557.

4 L. Dunsch and S. Yang, *Small*, 2007, **3**, 1298–1320.

5 M. N. Chaur, F. Melin, A. L. Ortiz and L. Echegoyen, *Angew. Chem., Int. Ed.*, 2009, **48**, 7514–7538.

6 H. Funasaka, K. Sakurai, Y. Oda, K. Yamamoto and T. Takahashi, *Chem. Phys. Lett.*, 1995, **232**, 273–277.

7 H. J. Huang, S. H. Yang and X. X. Zhang, *J. Phys. Chem. B*, 1999, **103**, 5928–5932.

8 R. Kitaura, H. Okimoto, H. Shinohara, T. Nakamura and H. Osawa, *Phys. Rev. B: Condens. Matter Mater. Phys.*, 2007, **76**, 172409.

9 H. J. Huang, S. H. Yang and X. X. Zhang, *J. Phys. Chem. B*, 2000, **104**, 1473–1482.

10 M. Wolf, K. H. Muller, D. Eckert, Y. Skourski, P. Georgi, R. Marczak, M. Krause and L. Dunsch, *J. Magn. Magn. Mater.*, 2005, **290**, 290–293.

11 F. Bondino, C. Cepek, N. Tagmatarchis, M. Prato, H. Shinohara and A. Goldoni, *J. Phys. Chem. B*, 2006, **110**, 7289–7295.

12 R. Westerström, J. Dreiser, C. Piamonteze, M. Muntwiler, S. Weyeneth, H. Brune, S. Rusponi, F. Nolting, A. Popov, S. Yang, L. Dunsch and T. Greber, *J. Am. Chem. Soc.*, 2012, **134**, 9840–9843.

13 M. Wolf, K. H. Muller, Y. Skourski, D. Eckert, P. Georgi, M. Krause and L. Dunsch, *Angew. Chem., Int. Ed.*, 2005, **44**, 3306–3309.

14 H. Okimoto, R. Kitaura, T. Nakamura, Y. Ito, Y. Kitamura, T. Akachi, D. Ogawa, N. Imazu, Y. Kato, Y. Asada, T. Sugai, H. Osawa, T. Matsushita, T. Muro and H. Shinohara, *J. Phys. Chem. C*, 2008, **112**, 6103–6109.

15 A. Tiwari, G. Dantelle, K. Porfyrakis, A. A. R. Watt, A. Ardavan and G. A. D. Briggs, *Chem. Phys. Lett.*, 2008, **466**, 155–158.

16 T. Zuo, M. M. Olmstead, C. M. Beavers, A. L. Balch, G. Wang, G. T. Yee, C. Shu, L. Xu, B. Elliott, L. Echegoyen, J. C. Duchamp and H. C. Dorn, *Inorg. Chem.*, 2008, **47**, 5234–5244.

17 B. Náfrádi, Á. Antal, Á. Pásztor, L. Forró, L. F. Kiss, T. Fehér, É. Kováts, S. Pekker and A. Jánossy, *J. Phys. Chem. Lett.*, 2012, **3**, 3291–3296.

18 C. F. Hermanns, M. Bernien, A. Krüger, C. Schmidt, S. T. Waßerroth, G. Ahmadi, B. W. Heinrich, M. Schneider, P. W. Brouwer, K. J. Franke, E. Weschke and W. Kuch, *Phys. Rev. Lett.*, 2013, **111**, 167203.

19 R. Westerström, J. Dreiser, C. Piamonteze, M. Muntwiler, S. Weyeneth, K. Krämer, S.-X. Liu, S. Decurtins, A. Popov, S. Yang, L. Dunsch and T. Greber, *Phys. Rev. B: Condens. Matter Mater. Phys.*, 2014, **89**, 060406.

20 A. L. Svitova, Y. Krupskaya, N. Samoylova, R. Kraus, J. Geck, L. Dunsch and A. A. Popov, *Dalton Trans.*, 2014, **43**, 7387–7390.

21 M. R. Cerón, F.-F. Li and L. A. Echegoyen, *J. Phys. Org. Chem.*, 2014, **27**, 258–264.

22 S. F. Yang, A. A. Popov, M. Kalbac and L. Dunsch, *Chem.–Eur. J.*, 2008, **14**, 2084–2092.

23 S. Stevenson, C. Chancellor, H. M. Lee, M. M. Olmstead and A. L. Balch, *Inorg. Chem.*, 2008, **47**, 1420–1427.

24 Y. Zhang, S. Schiemenz, A. A. Popov and L. Dunsch, *J. Phys. Chem. Lett.*, 2013, **4**, 2404–2409.

25 S. F. Yang, M. Kalbac, A. Popov and L. Dunsch, *ChemPhysChem*, 2006, **7**, 1990–1995.

26 Y. Zhang, A. A. Popov and L. Dunsch, *Nanoscale*, 2014, **6**, 1038–1048.

27 R. Shannon, *Acta Crystallogr., Sect. A: Cryst. Phys., Diffr., Theor. Gen. Crystallogr.*, 1976, **32**, 751–767.

28 Y. Zhang, A. A. Popov, S. Schiemenz and L. Dunsch, *Chem.–Eur. J.*, 2012, **18**, 9691–9698.

29 S. Stevenson, G. Rice, T. Glass, K. Harich, F. Cromer, M. R. Jordan, J. Craft, E. Hadju, R. Bible, M. M. Olmstead, K. Maitra, A. J. Fisher, A. L. Balch and H. C. Dorn, *Nature*, 1999, **401**, 55–57.

30 J. Zhang and H. C. Dorn, *Fullerenes, Nanotubes, Carbon Nanostruct.*, 2014, **22**, 35–46.

31 S. Yang, A. A. Popov and L. Dunsch, *Angew. Chem., Int. Ed. Engl.*, 2008, **47**, 8196–8200.

32 I. Bertini, C. Luchinat and G. Parigi, *Solution NMR of Paramagnetic Molecules. Application to Metallobiomolecules and Models*, Elseviser Science B. V., Amsterdam, 2001.

33 B. Bleaney, *J. Magn. Reson.*, 1972, **8**, 91–100.

34 B. Bleaney, C. M. Dobson, B. A. Levine, R. B. Martin, R. J. P. Williams and A. V. Xavier, *J. Chem. Soc., Chem. Commun.*, 1972, 791–793.

35 I. Bertini, M. B. L. Janik, Y.-M. Lee, C. Luchinat and A. Rosato, *J. Am. Chem. Soc.*, 2001, **123**, 4181–4188.

36 W. D. Horrocks Jr, *J. Magn. Reson.*, 1977, **26**, 333–339.

37 B. R. McGarvey, *J. Magn. Reson.*, 1979, **33**, 445–455.

38 V. S. Mironov, Y. G. Galyametdinov, A. Ceulemans, C. Görller-Walrand and K. Binnemans, *J. Chem. Phys.*, 2002, **116**, 4673–4685.

39 L. Zhang, A. A. Popov, S. Yang, S. Klod, P. Rapta and L. Dunsch, *Phys. Chem. Chem. Phys.*, 2010, **12**, 7840–7847.

40 X. L. Wang, T. M. Zuo, M. M. Olmstead, J. C. Duchamp, T. E. Glass, F. Cromer, A. L. Balch and H. C. Dorn, *J. Am. Chem. Soc.*, 2006, **128**, 8884–8889.

41 M. Yamada, T. Wakahara, T. Tsuchiya, Y. Maeda, T. Akasaka, N. Mizorogi and S. Nagase, *J. Phys. Chem. A*, 2008, **112**, 7627–7631.

42 M. Yamada, T. Wakahara, T. Tsuchiya, Y. Maeda, M. Kako, T. Akasaka, K. Yoza, E. Horn, N. Mizorogi and S. Nagase, *Chem. Commun.*, 2008, 558–560.

43 M. Yamada, N. Mizorogi, T. Tsuchiya, T. Akasaka and S. Nagase, *Chem.–Eur. J.*, 2009, **15**, 9486–9493.

44 B. T. Thole, P. Carra, F. Sette and G. van der Laan, *Phys. Rev. Lett.*, 1992, **68**, 1943–1946.

45 P. Carra, B. T. Thole, M. Altarelli and X. Wang, *Phys. Rev. Lett.*, 1993, **70**, 694–697.

46 J. Dreiser, R. Westerström, Y. Zhang, A. A. Popov, L. Dunsch, K. Krämer, S.-X. Liu, S. Decurtins and T. Greber, *Chem. Eur. J.*, 2014DOI: 10.1002/chem.201403042.

47 A. A. Granovsky, *Firefly,*version 8.0.0, 2013, http://classic.chem.msu.su/gran/firefly/index.html.

48 M. Rotter, *J. Magn. Magn. Mater.*, 2004, **272–276**, E481–E482.

49 T. A. Keith, in *AIMAll (Version 14.04.17)*, http://aim.tkgristmill.com, 2014.

50 A. A. Popov and L. Dunsch, *Chem.–Eur. J.*, 2009, **15**, 9707–9729.

51 V. Vieru, L. Ungur and L. F. Chibotaru, *J. Phys. Chem. Lett.*, 2013, **4**, 3565–3569.

52 T. Heine, K. Vietze and G. Seifert, *Magn. Reson. Chem.*, 2004, **42**, S199–S201.

53 J. VandeVondele, M. Krack, F. Mohamed, M. Parrinello, T. Chassaing and J. Hutter, *Comput. Phys. Commun.*, 2005, **167**, 103–128.

54 C. Piamonteze, U. Flechsig, S. Rusponi, J. Dreiser, J. Heidler, M. Schmidt, R. Wetter, M. Calvi, T. Schmidt, H. Pruchova, J. Krempasky, C. Quitmann, H. Brune and F. Nolting, *J. Synchrotron Radiat.*, 2012, **19**, 661–674.

55 V. V. Voevodin, S. A. Zhumatiy, S. I. Sobolev, A. S. Antonov, P. A. Bryzgalov, D. A. Nikitenko, K. S. Stefanov and V. V. Voevodin, in *Open Systems J. 2012*, http://www.osp.ru/os/2012/2007/13017641.